

**Design of high-temperature solar-selective coatings based on aluminium titanium oxynitrides  $\text{Al}_y\text{Ti}_{1-y}(\text{O}_x\text{N}_{1-x})$ . Part 1: Advanced microstructural characterisation and optical simulation**

Heras, I.; Guillén, E.; Lungwitz, F.; Rincón-Llorente, G.; Munnik, F.; Schumann, E.; Azkona, I.; Krause, M.; Escobar-Galindo, R.;

Originally published:

December 2017

**Solar Energy Materials and Solar Cells 176(2018), 81-92**

DOI: <https://doi.org/10.1016/j.solmat.2017.10.015>

Perma-Link to Publication Repository of HZDR:

<https://www.hzdr.de/publications/Publ-26727>

Release of the secondary publication  
on the basis of the German Copyright Law § 38 Section 4.

CC BY-NC-ND

# Design of high-temperature solar-selective coatings based on aluminium titanium oxynitrides $\text{Al}_y\text{Ti}_{1-y}(\text{O}_x\text{N}_{1-x})$ .

## Part 1: Advanced microstructural characterisation and optical simulation

I. Heras<sup>1</sup>, E. Guillén<sup>1\*</sup>, F. Lungwitz<sup>2</sup>, G. Rincón-Llorente<sup>1</sup>, F. Munnik<sup>2</sup>, E. Schumann<sup>2</sup>, I. Azkona<sup>3</sup>, M. Krause<sup>2</sup>, R. Escobar-Galindo<sup>1†</sup>

<sup>1</sup>Abengoa Research S. L., Abengoa, Seville, Campus Palmas Altas 41014, Spain.

<sup>2</sup>Helmholtz-Zentrum Dresden-Rossendorf, Bautzner Landstraße 400, 01328 Dresden, Germany.

<sup>3</sup>Metal Estalki S.L., Polígono Ugaldeguren II, 48170 Zamudio, Spain

### Abstract

Aluminium titanium oxynitrides were studied as candidate materials for high temperature solar-selective coatings due to their excellent stability and their tuneable optical behaviour. A set of individual  $\text{Al}_y\text{Ti}_{1-y}(\text{O}_x\text{N}_{1-x})$  layers with different oxygen content was prepared by cathodic vacuum arc (CVA) deposition. The composition, morphology, phase structure and microstructure of the films were characterized by elastic recoil detection (ERD), scanning and transmission electron microscopy and X-ray diffraction. An *fcc* phase structure is found in a broad compositional range of  $\text{Al}_y\text{Ti}_{1-y}(\text{O}_x\text{N}_{1-x})$ . Simultaneously, sample microstructure and morphology undergo systematic changes from a columnar growth to the development of a heterogeneous structure with spherical nanoparticle inclusions when the oxygen concentration is increased. The optical properties were determined by ellipsometry and UV-Vis-NIR- FTIR spectroscopy. A comprehensive analysis of the film properties allowed an accurate modelling of the optical constants of the  $\text{Al}_y\text{Ti}_{1-y}(\text{O}_x\text{N}_{1-x})$  in the whole wavelength range of solar interest (from 190 nm to 25  $\mu\text{m}$ ). It points to a transition from metallic to dielectric behaviour with increasing oxygen content. Consequently, it is demonstrated that the optical properties of these  $\text{Al}_y\text{Ti}_{1-y}(\text{O}_x\text{N}_{1-x})$  deposited films can be controlled in a wide range from metallic to dielectric character by adjusting the oxygen concentration, opening a huge range of possibilities for the design of solar selective coatings (SSC) based on this material. Complete SSC were designed by applying optical simulations, obtaining excellent optical selective properties of  $\alpha = 94.0\%$  and  $\varepsilon_{RT} = 4.8\%$ .

---

\* Present address: Profactor, Im Stadtgut A2 | 4407 Steyr-Gleink | Austria; elena.guillen@profactor.at

† Corresponding author: Tel +34 649 833 073; ramon.escobar@abengoa.com (R. Escobar-Galindo)

# 1 Introduction

Concentrating solar power (CSP) electricity generation is a commercially available technology capable of harvesting the solar resources in many parts of the world. CSP offers the possibility of incorporating thermal storage, providing dispatchable electrical power [1] that can compete with conventional fossil fuel plants [1]. A high-temperature heat source is created by concentrating the solar radiation reflected from the heliostats field onto a sunlight absorbing receiver. The thermal energy is converted into electricity downstream by a heat exchanger, steam turbine, and electrical power generator in a thermodynamic cycle. Solar selective coatings (SSC) with high absorptance ( $\alpha$ ) in the solar spectral range (0.3 – 2.5  $\mu\text{m}$ ) and low thermal emittance ( $\epsilon$ ) in the infrared region (2.5 – 30  $\mu\text{m}$ ) are required for improving the performance of CSP receivers [2]. SSC deposited by physical vapor deposition (PVD) techniques are currently applied in parabolic trough systems, working at temperatures below 400 °C and under vacuum environments [3]. In the case of central receivers of solar tower plants that operate at high temperatures in ambient conditions, commercial solutions based on absorber paints (i.e. Pyromark®) are currently applied. These paints exhibit no solar selectivity ( $\epsilon > 80\%$ ) and suffer from serious degradation at temperatures above  $> 550^\circ\text{C}$  [4,5]. Although there has been an extensive evaluation of PVD coatings in literature [6–10] the stringent operation conditions in central receiver towers have prevented to this date the commercial implementation of PVD based SSC.

PVD deposited nitride and oxynitride coatings are considered to have potential as solar absorber layers in high-temperature applications due to their excellent oxidation resistance [11] and thermal stability [12]. Related research has been extensively reported in the literature [13–19]. In 2009 Lei *et al.* [20], developed a multilayer stack including an AlTiO thin film as anti-reflective (AR) layer by multi-arc ion plating system using only one Al<sub>50</sub>Ti<sub>50</sub> cathode. They obtained a solar absorptance of  $\sim 90\%$  stable in air at 650°C and a thermal emittance below 8%. However, the removal of large size macroparticles ( $\sim 0.5\mu\text{m}$ ) deposited with this technique required a suitable post-deposition process step. Rebouta *et al.* [16,21] obtained remarkable results in 2012 depositing Al<sub>50</sub>Ti<sub>50</sub> oxynitride multilayer stacks by DC magnetron sputtering (DC-MS) and using a top antireflective layer of SiO<sub>2</sub> (refractive index  $n \sim 1.44$ ) deposited by plasma enhanced chemical vapour deposition (PECVD) in a different coating chamber. The system was thermally stable in air for 600 hours at a temperature up to 278°C, with no changes in the solar absorptance of 95% and thermal emittance of 6%. Barshilia's AlTiN/AlTiON multilayer coatings on Cu substrate with Si<sub>3</sub>N<sub>4</sub> ( $n \sim 2.00$ ) as AR layer exhibited 95% absorptance and 7% thermal emittance at 82°C [22]. They employed an Al<sub>50</sub>Ti<sub>50</sub> cathode

for the oxynitrides and a second Si cathode for the AR layer. The coatings showed no degradation of the optical properties after 50 hours in air at 525°C. The last two multilayer designs require a different cathode (Si) or deposition chamber for the AR layer, increasing the complexity of the system. Afterwards, in 2014, Barshilia designed a similar stack based on pure metallic Ti and Al cathodes [23,24], using a pulsed DC-MS system to control independently the composition of each layer. This new configuration includes AlTiO ( $n \sim 1.8$ ) as AR layer and Ti chrome as infrared (IR) reflecting layer. This system did not achieve the same optimal performance as the previous ones ( $\alpha = 93\%$  and  $\varepsilon_{82^\circ\text{C}} = 16\%$ ), but it is simpler to implement and represents a distinct step towards industrial applications. Following the same  $\text{Al}_y\text{Ti}_{1-y}(\text{O}_x\text{N}_{1-x})$  structure, in 2015 Barshilia's group added a W layer between the substrate and the  $\text{MeO}_x\text{N}_y$  multilayer stack and they managed to reduce the emittance and to avoid diffusion from the substrate to the coating up to 300°C [24]. Several patents were filed by Barshilia employing aluminium titanium oxynitride multilayer stacks [25,26] based on the previously explained results. In 2014, a hybrid system combining pulsed DC-MS  $\text{Al}_y\text{Ti}_{1-y}(\text{O}_x\text{N}_{1-x})$  stack with a sol-gel AR top layer of organically modified silica (ormosil) was patented [27].

The structure analysis of a broad number of  $\text{Al}_y\text{Ti}_{1-y}(\text{O}_x\text{N}_{1-x})$  samples has revealed two limiting cases. When the oxygen to nitrogen atomic ratio (O/N) is low ( $< \sim 0.3$  [28]), the O atoms can be incorporated in the osbornite B1 cubic structure ( $Fm\bar{3}m$  space group) replacing N. The incorporation of oxygen into the nitride lattice affects the properties of the compound due to different charges and differences in the nature of metal-anion bonds [29]. Two nitrogen atoms ( $\text{N}^{3-}$ ) need to be replaced by three oxygen atoms ( $\text{O}^{2-}$ ) in order to maintain the electrical neutrality. For  $\text{O/N} > 0.3$  content above this limit, other structural phases are expected to be formed [30].

While its phase structure can be predicted depending on the O/N ratio [31,32], the microstructural design of the  $\text{Al}_y\text{Ti}_{1-y}(\text{O}_x\text{N}_{1-x})$  system can be strongly influenced by the employed deposition technique and conditions. Structural and chemical properties of magnetron sputtered [33] and cathodic vacuum arc grown [30]  $\text{Al}_y\text{Ti}_{1-y}(\text{O}_x\text{N}_{1-x})$  have been studied, showing the improvement of the thermal resistance and mechanical properties with the addition of a certain oxygen content.

As we discussed in a previous work by some of the authors [34], the design of solar selective coatings requires a reliable simulation of the optimized coating stack followed by an experimental confirmation of the optical response. To achieve this, it is crucial to base the simulation on optical constants, which properly describe the optical behaviour of the material.

This represents a major difficulty for  $\text{Al}_y\text{Ti}_{1-y}(\text{O}_x\text{N}_{1-x})$  due to the strong dependence of the optical response on the composition and bonding behaviour of the material. Besides there is a very limited knowledge on the dependencies of optical properties in the IR range for the majority of optical materials. Therefore, one of the main objectives of this study is the proper determination of the optical constants of individual  $\text{Al}_y\text{Ti}_{1-y}(\text{O}_x\text{N}_{1-x})$  layers in the wavelength range of interest (300-25000 nm) supported by a detailed analysis of the film composition, microstructure and phase morphology. The second objective is to apply this optical model to the design of a complete stack of solar selective AR layer /  $\text{Al}_y\text{Ti}_{1-y}(\text{O}_x\text{N}_{1-x})$  absorber layers / IR reflector with optimized  $\alpha/\varepsilon$  ratio relevant for high-temperature applications.

For that aim, a set of individual layers grown by Cathodic Vacuum Arc (CVA) were thoroughly analysed in terms of composition using Elastic Recoil Detection (ERD) and Rutherford Backscattering Spectrometry (RBS), morphology by Scanning Electron Microscopy (SEM) and microstructure by X-ray diffraction (XRD) and transmission electron microscopy (TEM). Reflectance spectra were obtained by UV-Vis-NIR and FTIR spectrophotometry. An extensive modelling study was performed for the proper simulation of the optical constants measured by spectroscopic ellipsometry (SE). This led to excellent agreement between simulated and experimentally obtained reflectance spectra within the whole wavelength range of interest. In this work, it is demonstrated that a solid understanding of the correlations between bonding type and composition is required in order to properly adjust the solar selective properties of high-temperature resistance oxynitride materials. Based on this approach, a complete solar selective multilayer stack was optimized achieving optical properties ( $\alpha = 94.0\%$  and  $\varepsilon_{\text{RT}} = 4.8\%$ ) that are among the best performing reported for simulated layer stacks using oxynitride films [18,35]. In a companion paper [36] the thermal stability of the optimized complete multilayer stack in air were analysed by i) asymmetric tests of 12 hours at 450, 650 and 800°C and ii) heating– cooling cycles between 300-600°C for 900 hours.

## 2 Experimental details

### 2.1 Thin film growth

A set of  $\text{Al}_y\text{Ti}_{1-y}(\text{O}_x\text{N}_{1-x})$  thin films was deposited on Si (100) and mirror polished Inconel HAYNES ® 230 substrates using a commercial direct current (DC) non-filtered cathodic vacuum arc PL70 Platit setup. The common deposition parameters applied for the  $\text{Al}_y\text{Ti}_{1-y}(\text{O}_x\text{N}_{1-x})$  samples are summarized in Table 1.

Table 1: Common deposition parameters employed for  $\text{Al}_y\text{Ti}_{1-y}(\text{O}_x\text{N}_{1-x})$  samples grown by CVA PL70 Platit setup.

Parameter	Value
Base pressure (Pa)	$2 \times 10^{-4}$
Working pressure (Pa)	1.5
Deposition temperature ( $^{\circ}\text{C}$ )	450
Cathodes	$\text{Al}_{67}\text{Ti}_{33}$
Cathode size ( $\text{mm}^2$ )	331 x 174
Discharge current (A)	125
Bias voltage at deposition stage (V)	- 75
Rotation speed of the substrate (rpm)	10
Distance to the substrate (mm)	150

As they were optimized previously for similar nitride films in this CVA chamber [28,37], the substrate temperature (450  $^{\circ}\text{C}$ ), the arc current (125 A) and the substrate bias (-75 V) were kept as constant parameters in order to obtain samples with low residual stress and good adhesion. A single rectangular  $\text{Al}_{67}\text{Ti}_{33}$  cathode was employed for all the depositions. The flow rate of the reactive gases  $\text{O}_2$  and  $\text{N}_2$  was varied. In this way, six  $\text{Al}_y\text{Ti}_{1-y}(\text{O}_x\text{N}_{1-x})$  thin film samples were obtained. They are abbreviated by the notation #1 to #6 in the following text (see Table 2Table 3).

Table 2: Gas flow parameters applied for  $\text{Al}_y\text{Ti}_{1-y}(\text{O}_x\text{N}_{1-x})$  thin films deposition.

Sample	Coating type	Flow rates (sccm)			$\text{O}_2/(\text{O}_2+\text{N}_2)$ gas flow ratio (%)
		Ar	$\text{N}_2$	$\text{O}_2$	
1	AlTiN	0	70	0	0
2	$\text{Al}_y\text{Ti}_{1-y}(\text{O}_x\text{N}_{1-x})$	0	72	3	4.0
3		0	61	5	8.0
4		0	52	8	13.0
5		0	46	12	21.0
6	AlTiO <sub>x</sub>	10	0	50	100.0

Samples #1 - #5 were grown using only reactive gases ( $\text{N}_2$  and  $\text{O}_2$ ) without Ar gas assistance. The pure oxide film (sample #6) was deposited to be used as AR top layer and to improve integrity and environmental protection at high temperatures [38]. For its deposition, 10 sccm of Ar gas flow was added to the chamber to stabilize the arc. Oxynitride samples #2-#5 were deposited on top of  $\sim 0.5 \mu\text{m}$  AlTiN in order to improve the layer adhesion to the substrate. No delamination was observed in any of the deposited thin films.

## 2.2 Thin films compositional and microstructural characterization

ERD analysis was used to determine the depth-resolved elemental composition of the samples #1 to #6. The measurements were carried out using an incident 43 MeV  $\text{Cl}^{7+}$  ion beam of a 6 MV tandem accelerator. The angle between the sample normal and the incoming beam is  $75^\circ$  and the scattering angle is  $31^\circ$  relative to the beam direction. The analysed area is about  $1.5 \times 1.5 \text{ mm}^2$ . The recoils have been detected with a Bragg ionization chamber using a full energy detection circuit for the ion energies and a fast timing circuit to obtain a Z-dependent signal (Z: atomic number) to separate ion species. Hydrogen has been detected with a separate solid state detector covered by an  $18 \text{ }\mu\text{m}$  Al foil to stop other scattered ions and recoils at a scattering angle of  $41^\circ$ . With this experimental configuration the ERD spectra of all elements are obtained, and moreover the RBS spectrum of Ti (and possible heavy element impurities). All spectra were fitted simultaneously using the program NDF v9.3g [39].

A Hitachi S5200 Scanning Electron Microscope (SEM) equipped with a field emission gun (FEG) was employed to analyse the morphology of the deposited samples. Cross sectional images of the samples deposited on silicon substrates were measured without metallization at 1 and 5 kV electron beam energy.

The phase structure of the thin films was determined by X-ray diffraction employing grazing incidence geometry (GIXRD) using a Rigaku Ultima IV diffractometer with  $\text{Cu-K}_\alpha$  radiation ( $\lambda=1.5406 \text{ \AA}$ ). The incident angle was  $0.4^\circ$ , and the XRD patterns were measured in the diffraction angle range of  $20\text{--}100^\circ$  in steps of  $0.02^\circ$ . The crystallite size was estimated employing the Scherrer equation with  $k$  of 0.94 [40].

The microstructure was analysed by cross-sectional transmission electron microscopy (TEM) with a TECNAI F30 microscope operated at 300 kV accelerating voltage. It is equipped with Schottky-type field emission gun and an ultra-high resolution pole piece. The thin lamellas required for the cross-section analysis were made using a Focused Ion Beam (FIB) Dual Beam Helios 650. It is equipped with a 30 kV Ga focused ion beam source combined with a 30kV electron beam placed at  $52^\circ$  between them, and with the Omniprobe® manipulator. Sample-protecting Pt thin films were deposited by electron beam deposition of  $(\text{CH}_3)_3(\text{C}_p\text{CH}_3)\text{Pt}$ .

## 2.3 Determination of optical properties

The optical constants of the deposited thin films were determined by spectroscopic ellipsometry (SE) in the wavelength range of 211 to 1688 nm using a rotating compensator ellipsometer M-2000FI (J. A. Woollam, Inc.) with a fixed angle of polarized light incidence

and reflection of 75°. The data were acquired and interpreted via modelling using WVASE32 software [41].

The specular reflectance at room temperature was measured in the range 190 to 3300 nm using a Perkin Elmer UV-Vis-NIR spectrophotometer Lambda 1050 under an incident angle of 11° from the normal. The system is equipped with a deuterium (175-320 nm) and a tungsten-halogen lamp (320–3300 nm). For rough samples, a 150 mm integrated sphere accessory consisting of two hemispheres coated with Spectralon and equipped with photomultiplier tube (PMT) and InGaAs detectors, was employed. Spectralon was employed as diffusively reflecting reference.

Measurements of the reflectance in the IR range were carried out with a Fourier transform infrared (FTIR) spectrometer Bruker Vertex 70. It is equipped with a DLaTGS detector and KBr beam splitter. The measurement range was 400 to 4000 cm<sup>-1</sup> (2.5 to 25 μm), and the resolution was 0.4 cm<sup>-1</sup>. A specular “W-type” accessory is employed to measure reflectance of mirror like samples, employing a gold coated glass as reference. Additionally, the IR reflectance of rough samples was measured by an integrated sphere accessory coated with gold.

The commercial software CODE [42] and WVASE32 [41] were employed to simulate the reflectance spectra.

The solar absorptance ( $\alpha$ ) and the thermal emittance ( $\varepsilon$ ) of the coatings can be evaluated from UV-Vis-NIR and FTIR reflectance spectra.  $\alpha$  is defined as the fraction of incident radiation in the solar wavelength range that is absorbed, and it is calculated according to equation (1) [43]:

$$\alpha = \frac{\int_{\lambda_1}^{\lambda_2} [1-R(\lambda)] G(\lambda) d\lambda}{\int_{\lambda_1}^{\lambda_2} G(\lambda) d\lambda} \quad (1)$$

where  $\lambda_1 = 300$  nm and  $\lambda_2 = 2500$  nm denote the integration limits,  $R(\lambda)$  the spectral reflectance, and  $G(\lambda)$  is the reference solar spectrum AM 1.5.  $\varepsilon$  is calculated applying Kirchhoff's law from the reflectance spectra in the infrared region, following equation (2):

$$\varepsilon(T) = \frac{\int_{\lambda_1}^{\lambda_2} [1-R(\lambda, T)] B(\lambda, T) d\lambda}{\int_{\lambda_1}^{\lambda_2} B(\lambda, T) d\lambda}, \quad (2)$$

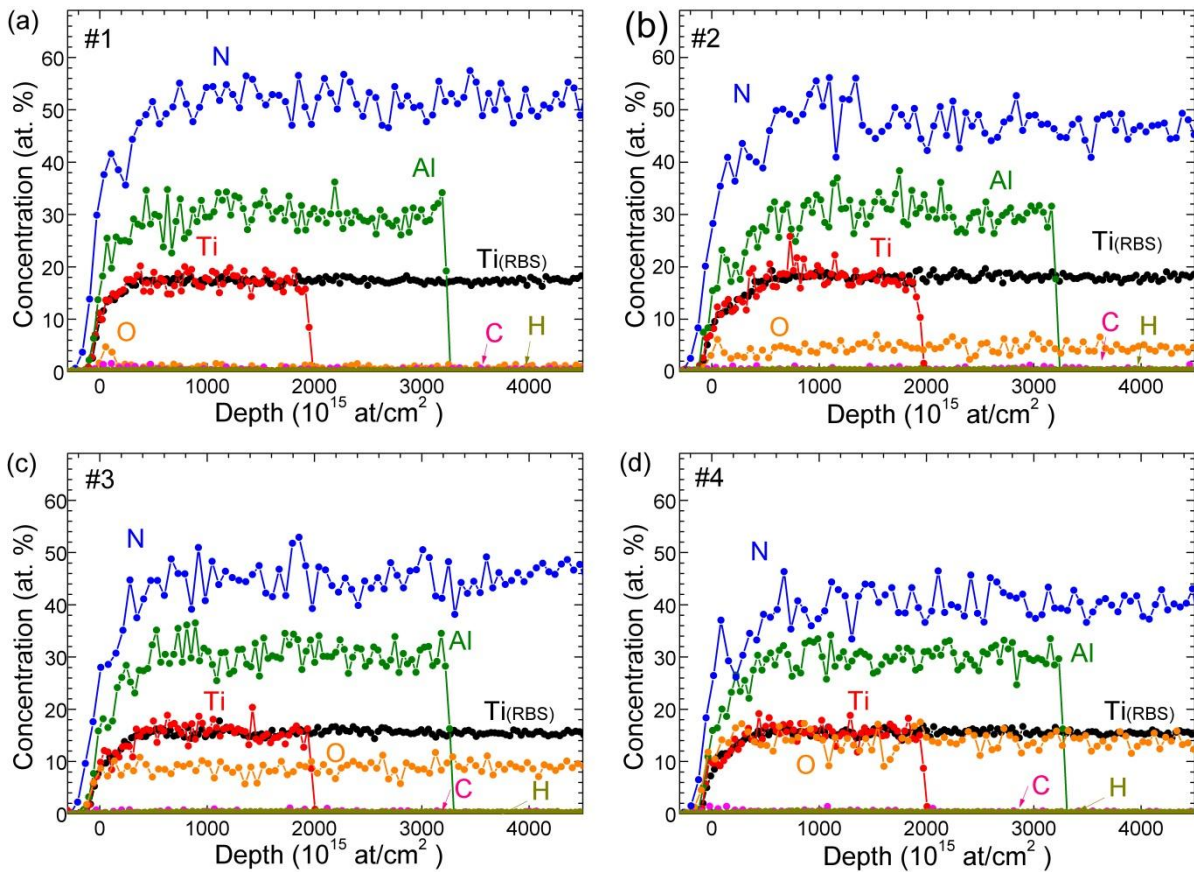
where  $B(\lambda, T)$  is the spectral distribution of the blackbody radiation calculated with Plank's law [44] for a specific temperature  $T$  in Kelvin degrees. The integration interval is limited by  $\lambda_1 = 1$  μm and  $\lambda_2 = 25$  μm, based on European standard EN-673:2011 [45].



### 3 Results and discussion

#### 3.1 Film composition and depth profile

The ERD elemental depth profiles of the  $\text{Al}_y\text{Ti}_{1-y}(\text{O}_x\text{N}_{1-x})$  samples #1 to #6 are displayed in Figure 1 (a) to (f). The thickness in atoms/cm<sup>2</sup> is directly obtained from the measurements. The depth profiles are based on the recoil spectra except for Ti, for which also the profile based on the  $\text{Cl}^{+7}$  backscattering spectrum (marked as Ti (RBS)) is displayed in order to increase the information depth for this element. The analysis depth limit is different for each element due to limitations in the separation of each recoil ion from the scattered Cl ions. It is reflected in the graph by the abrupt drop of the ERD intensity. Sample #6 is the only sample where the Si substrate was detected (Figure 1 (f)) due to its lower thickness (85 nm) compared to samples #1-#5 ( $d > 1.0 \mu\text{m}$ ). In the near surface region the depth profiles do not add up to 100%. This effect is caused by surface roughness which causes that the spectra are more rounded in the surface region compared to the simulation without surface roughness [46].



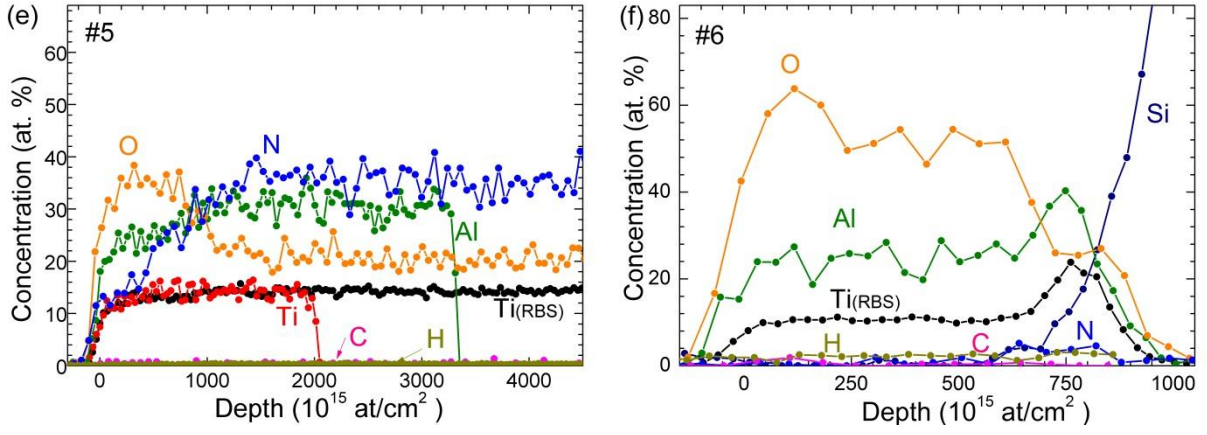


Figure 1: Elemental depth profiles of samples #1 to #6 analysed by ERD.

The elemental concentration of the samples #1 to #6 measured by ERD analysis is summarized in Table 3. These values were obtained from the deeper part of the samples where the film composition is homogeneous.

Table 3: Elemental composition of  $\text{Al}_y\text{Ti}_{1-y}(\text{O}_x\text{N}_{1-x})$  thin films. The estimated uncertainty is  $\pm 0.5$  at. %.

#	Coating type	Elemental composition (at.%)						O/(O+N)	Al/(Al+Ti)	(Al+Ti)/(Total)
		O	N	Ti	Al	C	H	(%)	(%)	(%)
1	AlTiN	0.5	52.0	17.0	30.0	0.5	0.0	$1 \pm 1$	$64 \pm 1$	$47 \pm 2$
2	$\text{Al}_y\text{Ti}_{1-y}(\text{O}_x\text{N}_{1-x})$	4.5	47.0	18.0	30.0	0.5	0.0	$9 \pm 1$	$63 \pm 1$	$48 \pm 2$
3		9.0	45.0	16.0	30.0	0.0	0.0	$17 \pm 1$	$65 \pm 1$	$46 \pm 2$
4		14.0	40.0	16.0	30.0	0.0	0.0	$26 \pm 1$	$65 \pm 1$	$46 \pm 2$
5		20.0	35.0	14.0	30.0	0.5	0.5	$36 \pm 2$	$68 \pm 1$	$44 \pm 2$
6	AlTiO <sub>x</sub>	58.0	1.0	10.0	27.0	3.0	1.0	$100 \pm 3$	$73 \pm 1$	$38 \pm 2$

As shown in Table 3, the H and C concentration in the  $\text{Al}_y\text{Ti}_{1-y}(\text{O}_x\text{N}_{1-x})$  samples are close to the detection limit and independent of the reactive gases ratio or the operating pressure. The most remarkable observation is the substitution of nitrogen by oxygen in the oxynitride series (#1-5) with increasing  $\text{O}_2/(\text{O}_2+\text{N}_2)$  gas flow ratio (Figure 2). The oxygen to nitrogen content  $\text{O}/(\text{O}+\text{N})$  of the samples increases linearly from  $1 \pm 1$  % in the AlTiN sample #1 to  $36 \pm 2$  % in the oxynitride sample #5. Moreover, oxygen enrichment by a factor of approximately 2 is observed in all the oxynitride series #1 to #5 compared to the composition of the reactive gas. The uniform oxygen enrichment factor and the linear relationship between oxygen content in the reactive gas atmosphere implies a similar structure-determining film growth mechanism in the samples #1 to #5. Otherwise a change in the slope or even kinks in the film composition vs. gas flow ratio relations might occur. These observations point to the incorporation of oxygen in the *fcc*-lattice rather than to a phase separation.

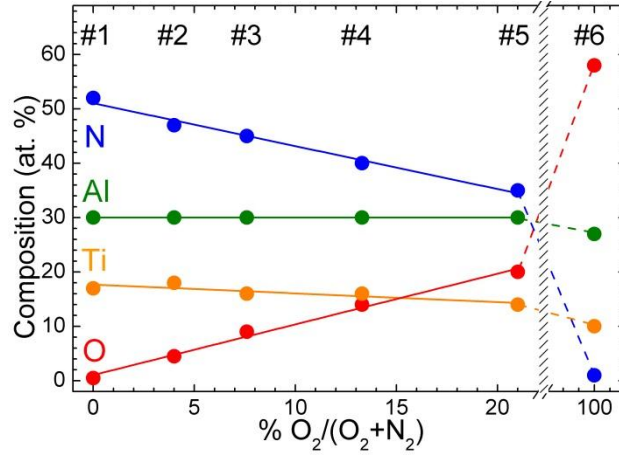


Figure 2: Al, Ti, N and O concentration of  $\text{Al}_y\text{Ti}_{1-y}(\text{O}_x\text{N}_{1-x})$  samples for different  $\text{O}_2 / (\text{O}_2 + \text{N}_2)$  reactive gas flow ratios, measured by ERD analysis.

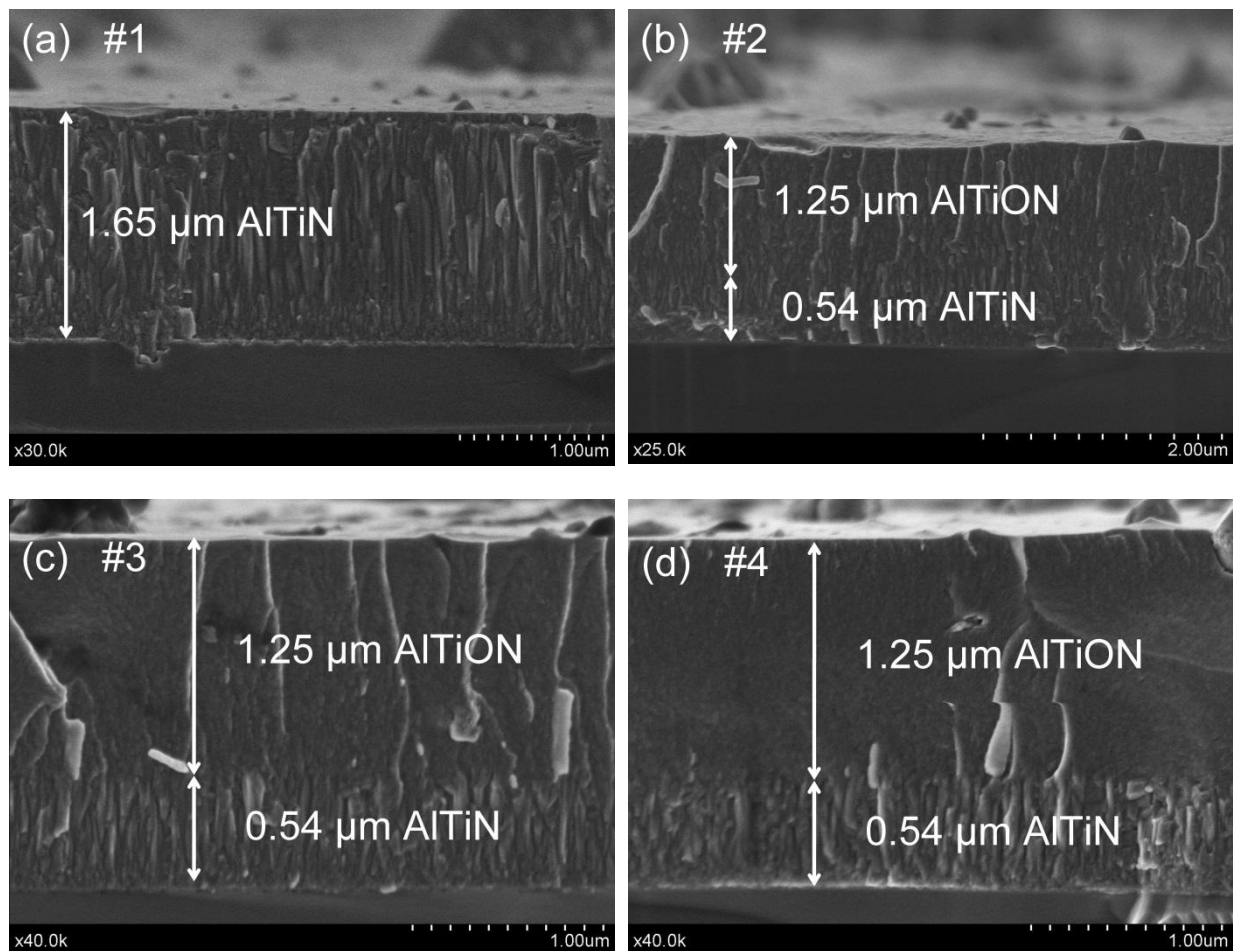
In samples #1 to #5 the Al and Ti content remains almost constant, with minor deviations of the Al:Ti ratio when compared to the cathode composition (67:33). The pure nitride sample (#1) has an oxygen impurity level of  $< 1$  at. % O. The precise stoichiometry of  $\text{Al}_{0.3}\text{Ti}_{0.17}\text{N}_{0.52}$  reveals a slight excess of nitrogen that might be indicative for the formation of metal vacancies in the cubic lattice. As the oxygen flow increases (samples #2-#5), the metallic proportion (i.e.  $(\text{Al}+\text{Ti})/(\text{Al}+\text{Ti}+\text{N}+\text{O})$ ) decreases from  $48 \pm 2\%$  in sample #2 to  $44 \pm 2\%$  in sample #5. Accordingly, the ratio metal to non-metal element  $(\text{Ti}+\text{Al}):(\text{N}+\text{O})$  decreases from  $0.93 \pm 0.04$  in sample #2 to  $0.80 \pm 0.03$  in sample #5.

The ERD spectrum of sample #6 shows three layers with different ratios of Al, Ti and O. The top layer practically has the stoichiometric  $(\text{Al,Ti})_2\text{O}_3$  composition, with 37 at.% of metal versus 58 at.% of oxygen. Its Al:Ti ratio of approximately 75:25 differs significantly from the initial cathode composition. There is a clear change in the slope of the oxygen and nitrogen gas flow ratio vs. film composition relations that may indicate a change in the structure-determining film growth mechanism of sample #6 as compared to samples #1 to #5. All these observations suggest the formation of either a mixture of  $(\text{Al}_{0.66}\text{Ti}_{0.33})_2\text{O}_3$  oxide along with free alumina  $\text{Al}_2\text{O}_3$  or a uniform mixed-metal oxide of the composition  $(\text{Al}_{0.75}\text{Ti}_{0.25})_2\text{O}_3$ . These three layers will be later included in the optical modelling of the sample.

### 3.2 Film morphology

SEM analysis of the cross-sectional morphology revealed the dependence of the coating structure of  $\text{Al}_y\text{Ti}_{1-y}(\text{O}_x\text{N}_{1-x})$  on the oxygen content (Figure 3). A pronounced dense columnar microstructure is observed for the oxygen-free AlTiN (sample #1), whose columns were grown throughout the whole film thickness. The microstructure of the oxynitride samples #2-#5 (Figure 3 (b)-(e)) is gradually affected by the oxygen content. The columnar structure is

progressively less evident and not detectable for samples #4 and #5 indicating very fine grained film morphology. It is known that a small concentration of oxygen can significantly modify the morphology of thin film, promoting re-nucleation during growth and formation of smaller grains [28]. For the pure oxide sample (Figure 3 (f)) no columnar growth was observed, but a heterogeneous structure developed with spherical nanoparticle inclusions (size ~10-30 nm). The SEM cross section revealed the presence of three different layers in the film with individual thicknesses, from top to bottom, of 16, 52 and 17 nm ( $\pm 3$  nm) respectively. This result is in accordance with the ERD profile of Figure 1 (f) and it will be included in the optical modelling of the sample (see section 3.4).).





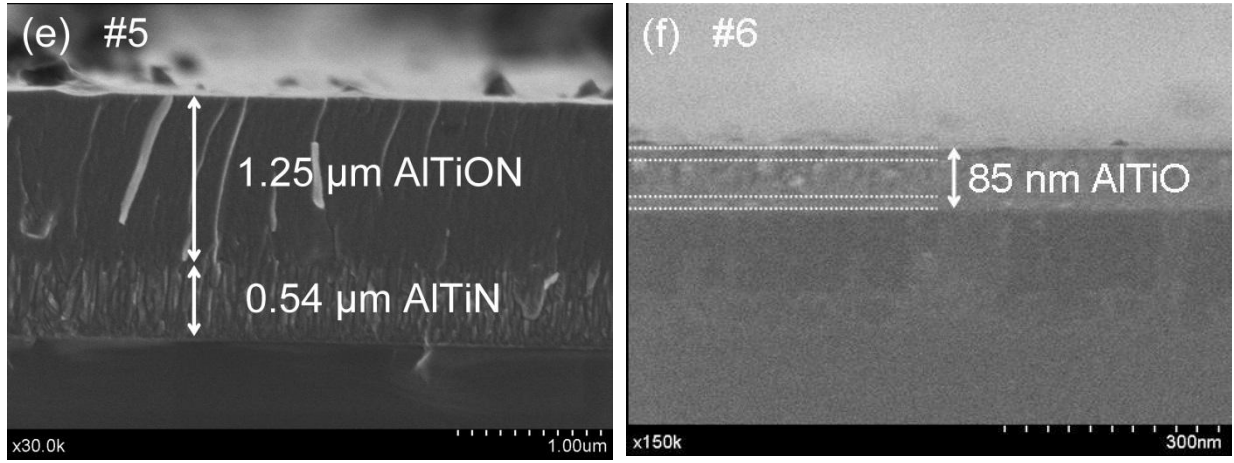


Figure 3: SEM cross-section images of  $\text{Al}_y\text{Ti}_{1-y}(\text{O}_x\text{N}_{1-x})$  films with different oxygen content on Si substrate. Samples #2, #3, #4, and #5 were deposited on top of  $\sim 0.5 \mu\text{m}$  AlTiN film. Sample #6 is deposited directly on the Si substrate.

Based on preliminary optical simulations of complete SSC (results not shown here), a more detailed microstructural and optical analysis was performed on selected samples (AlTiN #1, AlTiO #4, AlTiO #5 and AlTiO #6) as they were the most promising candidates to form a SSC multilayer stack showing a clear contrast in their optical properties. The phase structure and microstructure of these selected samples were analysed by XRD and TEM (section 3.3) while the optical constants of the films were obtained using spectroscopic ellipsometry modelling (section 3.4). After a complete comprehensive analysis, a complete SSC was finally designed with optimized optical performance (section 3.5).

### 3.3 Phase and microstructure of selected $\text{Al}_y\text{Ti}_{1-y}(\text{N}_{1-x}\text{O}_x)$ samples

The GIXRD patterns of selected  $\text{Al}_y\text{Ti}_{1-y}(\text{O}_x\text{N}_{1-x})$  films are represented in Figure 4. The crystallite sizes obtained from Scherrer's formula [47], interplanar spacing ( $d$ ) and lattice constants ( $a$ ) were calculated as an average of the main observed peaks and they are summarized in Table 4.

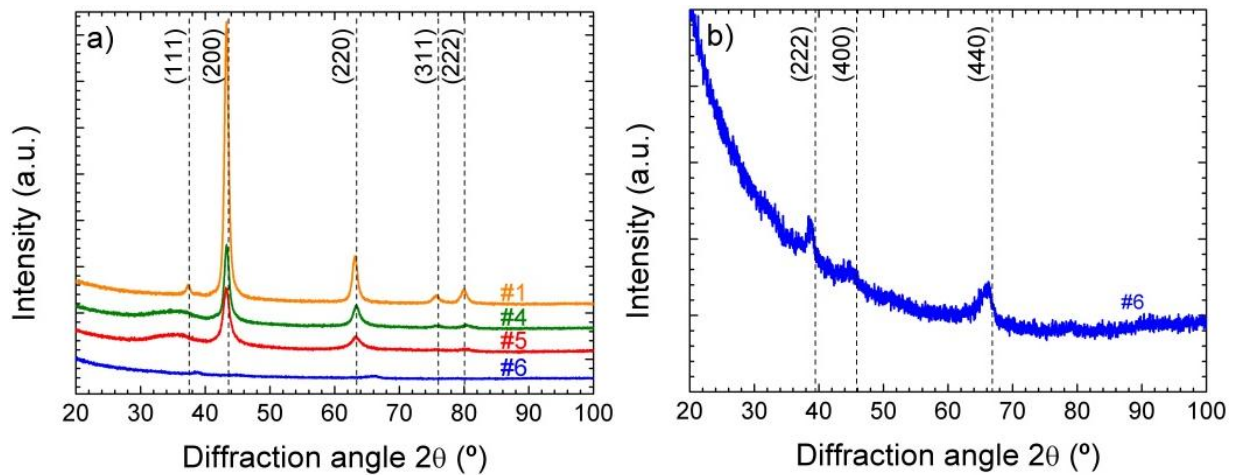


Figure 4: (a) GIXRD patterns of  $\text{Al}_y\text{Ti}_{1-y}(\text{O}_x\text{N}_{1-x})$  #1, #4, #5 and #6 samples. The vertical lines indicate the peak positions for  $\text{fcc-Al}_{0.5}\text{Ti}_{0.5}\text{N}$  (ICCD card number 04-018-6856) (b) Zoom-in of the GIXRD pattern of sample #6  $\text{AlTiO}$ . The vertical lines indicate the peak positions for  $\gamma\text{-Al}_2\text{O}_3$  (ICCD card number 00-056-0057).

Table 4: Structure data for selected  $\text{Al}_y\text{Ti}_{1-y}(\text{O}_x\text{N}_{1-x})$  thin films on Si substrate obtained from XRD patterns. The lattice constants ( $a$ ) were calculated by averaging the given values of the interplanar spacing ( $d$ ). Data of  $\text{fcc-Al}_{0.5}\text{Ti}_{0.5}\text{N}$  (ICCD card number 04-018-6856),  $\text{fcc-TiN}$  (ICCD card number 00-038-1420) and  $\gamma\text{-Al}_2\text{O}_3$  (ICCD card number 00-056-0057) are also shown as reference.

Sample #	Crystallite size (nm) average	$d$ (Å)	$(h\ k\ l)$	$a$ (Å) average
1	$11 \pm 1$	2.407	(111)	$4.17 \pm 0.01$
		2.090	(200)	
		1.473	(220)	
4	$8 \pm 2$	---	(111)	$4.16 \pm 0.02$
		2.088	(200)	
		1.467	(220)	
5	$6 \pm 3$	---	(111)	$4.17 \pm 0.02$
		2.091	(200)	
		1.469	(220)	
6	$5 \pm 2$	2.326	(222)	$8.06 \pm 0.03$
		2.022	(400)	
		1.419	(440)	
$\text{Al}_{0.5}\text{Ti}_{0.5}\text{N}$	---	2.395	(111)	4.15
		2.074	(200)	
		1.467	(220)	
TiN	---	2.449	(111)	4.24
		2.121	(200)	
		1.500	(220)	
$\gamma\text{-Al}_2\text{O}_3$	---	2.284	(222)	7.91
		1.978	(400)	
		1.398	(440)	

The diffractogram of the  $\text{AlTiN}$  (#1) and the  $\text{Al}_y\text{Ti}_{1-y}(\text{N}_{1-x}\text{O}_x)$  samples #4 and #5 showed a pattern corresponding to a face-centred cubic B1 structure (space group 225,  $Fm\text{-}3m$ ) (Figure 4). The observed peaks at  $2\theta = 37.3, 43.3, 63.1, 75.6$  and  $79.9^\circ$  are associated to the crystal planes (111), (200), (220), (311) and (222), respectively. This structure is typical for pure TiN and titanium-based nitrides. The formation of this structure in #1 and #4 is in agreement with literature data for  $\text{Al}_y\text{Ti}_{1-y}\text{N}$  samples wherein  $y \leq 0.67$  [48]. Interestingly, also sample #5 with  $y = 0.68 \pm 0.01$  adopts the same crystal structure. In the literature, a structure consisting of a mixture of cubic and hexagonal phase [37] or of  $h\text{-AlN}$  incorporated in a cubic  $\text{TiAlN}$  matrix

was reported for  $0.67 < y < 0.75$  [49]. No wurtzite structure was observed in the samples #1, #4 and #5 with  $y = 0.64$ ,  $0.65$ , and  $0.68$ , respectively.

The measured lattice constants of these rocksalt-type samples ( $4.17 \pm 0.01$  Å) are slightly larger than the reference value of  $\text{Al}_{0.5}\text{Ti}_{0.5}\text{N}$  ( $4.15$  Å, ICDD card 04-018-6856) and smaller than the reference value of TiN ( $4.24$  Å, ICDD card 00-038-1420). These results suggest that titanium atoms in the TiN lattice are statistically substituted by Al atoms with smaller atomic radius [50]. The slightly larger lattice constant compared to  $\text{Al}_{0.5}\text{Ti}_{0.5}\text{N}$  might indicate some degree of compressive strain. A progressive peak broadening is observed with increasing oxygen concentration, and the estimated crystallite sizes indicate a nanocrystalline microstructure for these three samples. Since microstrain cannot be excluded as source of line broadening, these numbers represent minimum values for the crystallite sizes. The XRD pattern of #4 and #5 showed one single additional broad (FWHM  $\sim 5^\circ$ ) diffraction feature around  $2\theta \sim 35^\circ$ . Because of its large width it could correspond to some amount of amorphous phase within these samples [30].

Finally, the pure oxide coating (sample #6) has a structure that resembles to metastable cubic  $\gamma\text{-Al}_2\text{O}_3$  phase with small peaks at  $2\theta = 38.7^\circ$ ,  $44.8^\circ$  and  $65.7^\circ$  corresponding to (222), (400) and (440), respectively, of the cubic structure (ICDD card 00-056-0457). The measured lattice constant  $a$  ( $8.06 \pm 0.03$  Å), is very similar to the reference unit cell parameters ( $a = b = c = 7.91$  Å). No other oxide crystalline phases (i.e.  $\text{TiO}_2$  or  $\text{Al}_2\text{TiO}_5$ ) were observed.

The TEM image of the AlTiN sample #1 (Figure 5 (a)) shows a clear columnar growth only interrupted by defects attributed to the release of macroparticles during the deposition process (see arrow in Figure 5 (a)) [51].

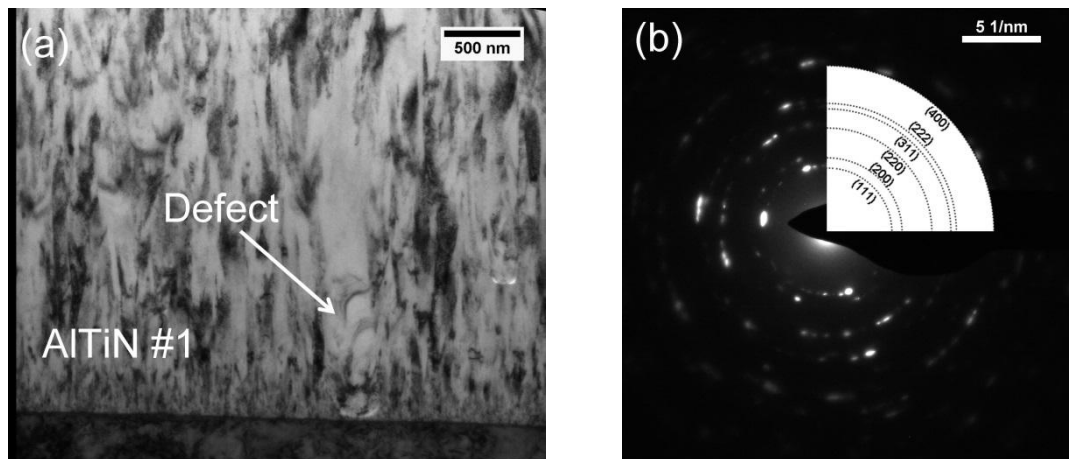
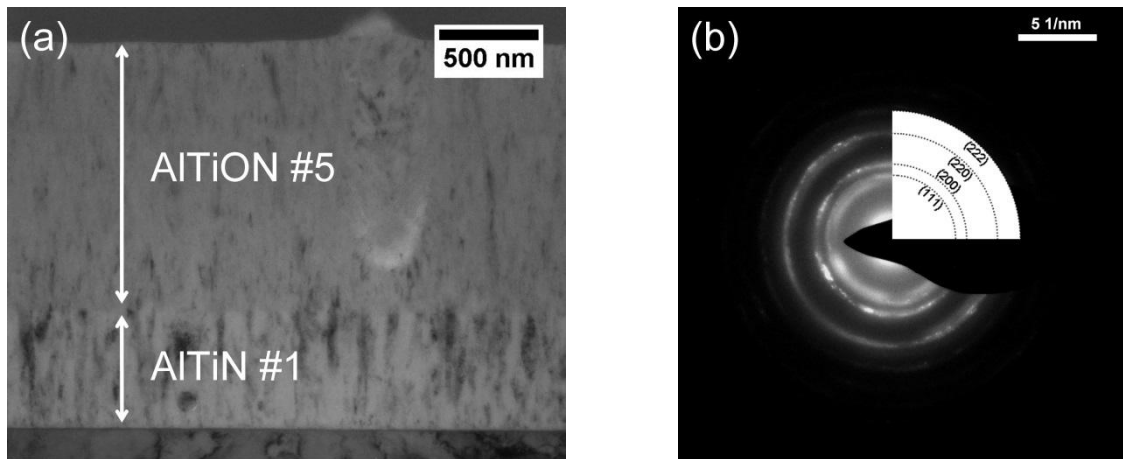


Figure 5: (a) TEM cross-section images of AlTiN sample #1 deposited on Inconel A defect assigned to a macroparticle loss is indicated. (b) Selected area electron diffraction pattern of (a).

The polycrystalline structure of AlTiN revealed by the Selective Area Electron Diffraction (SAED) pattern (Figure 5 (b)) shows six spotty-ring pattern corresponding to lattice plane distances of 2.4, 2.1, 1.5, 1.3, 1.2 and 0.9 Å, in good agreement with (111), (200), (220), (311), (222) and (400) reference values of *fcc*-Al<sub>0.5</sub>Ti<sub>0.5</sub>N (ICCD card 04-018-6856) and the XRD results shown in Table 4.

TEM images of AlTiON sample #5 are shown in Figure 6. The abrupt change of morphology and image contrast at a thickness of 500 nm corresponds to the interface between AlTiN and AlTiON. The AlTiON part has significantly less contrast than the AlTiN one, what is indicative for smaller grain sizes. As previously observed in SEM images, the addition of oxygen significantly modifies the morphology of the oxynitride film. It promotes renucleation during film growth and the formation of smaller grains as shown in Figure 6 (a).

The presence of four diffraction rings with varying sharpness in the SAED pattern of sample #5 (Figure 6 (b)), indicates the superposition of very small and randomly oriented crystallites and the presence of amorphous regions. There are very few spots visible in the rings in agreement with the reduction of the grain size observed by XRD. The interplanar distances calculated from SAED are 2.5, 2.1, 1.5 and 1.2 and correspond to (111), (200), (220), and (222) planes of *fcc*-Al<sub>0.5</sub>Ti<sub>0.5</sub>N (ICCD card 04-018-6856), respectively. No evidence of crystalline Al<sub>2</sub>O<sub>3</sub> or TiO<sub>2</sub> was observed.





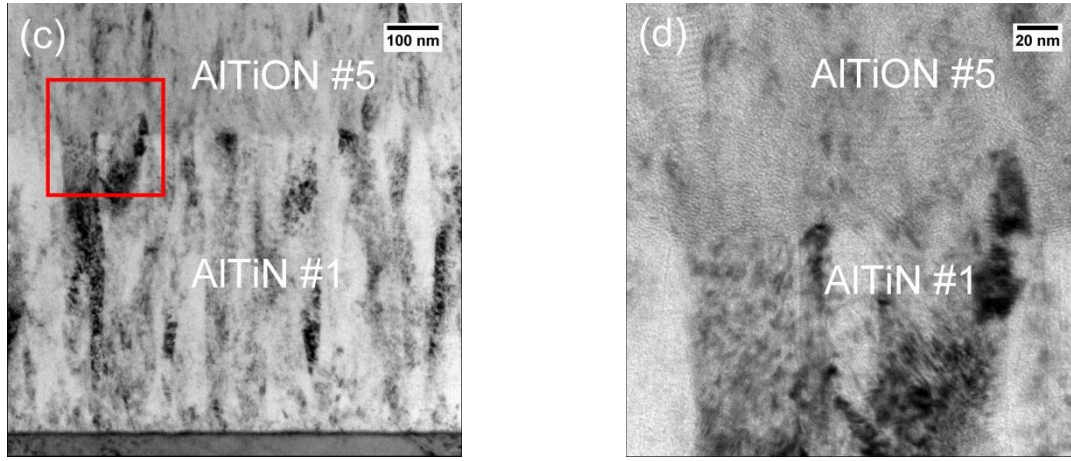


Figure 6: HR-TEM cross-section images of AlTiON#5 sample deposited on Inconel. (a) Overview image including the AlTiON and AlTiN layers. (b) Selected area electron diffraction pattern of AlTiON region of (a). (c) and (d) Magnified images of the interface region between AlTiN and AlTiON.

Higher resolution images of the film interface are displayed in Figure 6 (c) and (d). From these images it can be inferred that the columnar structure in the AlTiN serves as a template for promoting the pseudomorphic growth of the AlTiON layer [30,52]. Figure 6 (d) reveals a periodic multilayer structure within the AlTiON film with a periodicity of  $\sim 2$  nm. A similar multilayer structure with small columnar grains was described by Sjölen for equivalent CVA system [30], associated with rotation of the substrate holder during the deposition.

Based on the compositional and structural analysis the following summary of the microstructure evolution in  $\text{Al}_y\text{Ti}_{1-y}(\text{N}_{1-x}\text{O}_x)$  samples under study can be given. The linear relationship between oxygen content and oxygen gas flow without abrupt changes is a first hint for an identical structure-determining film formation process. The continuous variation of the composition is accompanied by an identical phase structure, namely the formation of a rocksalt-type lattice. Apparently, the *fcc*-AlTiN lattice is stable up to Al/Ti ratios of up to 0.68, what is among the highest values reported for this material system. Simultaneously the mean crystallite size is reduced from 11 nm for  $x = 0$  to 6 nm for  $x = 0.2$ . This can be attributed to a higher nucleation rate and lower surface diffusivity with increasing oxygen content. Hence, it was demonstrated that the nitrogen concentration in this type of films can be reduced by increasing the oxygen, while the stable *fcc* phase structure is conserved. The evolution of the material microstructure with increasing the O content was schematized in [53]. This approach can be used for the deposition of SSC stacks combining the high stability of the *fcc*-AlTiN lattice structure with the better oxidation resistance of oxygen enriched layers. The high solar absorptance expected from graded SSC based on  $\text{Al}_y\text{Ti}_{1-y}(\text{O}_x\text{N}_{1-x})$  films is attributed to these

morphological changes, as schematized at Figure 7. The solar absorption is related to light-matter interaction mechanisms, including photon-induced electronic transitions, and photon-induced collective electron oscillations in the AlTiN nanocrystallites [54, 55]. This multilayer structure consisting of layers with graded oxygen concentration is expected to be very efficient for solar selectivity [10,56].

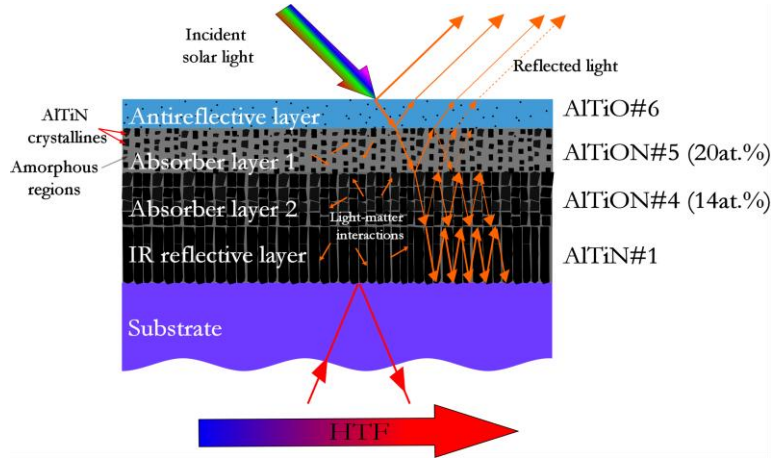


Figure 7: Schematic diagram of the reflectance as interference sum of multiples reflections of the interfaces and multiple scattering effects in AlTiO/AlTiON/AlTiN multilayer SSC stack. HTF stands for Heat Transfer Fluid.

### 3.4 Optical characterization and modelling of $Al_yTi_{1-y}(N_{1-x}O_x)$ samples

A proper analysis of the optical constants is crucial to succeed in the design of the multilayer SSC. After a detailed microstructural and morphological analysis, a new set of  $Al_yTi_{1-y}(N_{1-x}O_x)$  samples was deposited with the same process parameters as described in section 2.1 on silicon substrates and without AlTiN buffer layer for more precise optical analysis. The optical properties of the selected  $Al_yTi_{1-y}(O_xN_{1-x})$  films were analysed by SE in the range of 211 - 1688 nm. In order to extend them into the IR range, the reflectance spectra were measured for  $\lambda = 190 - 25000$  nm and included into the optical model.

Figure 8 (a-c) shows the SE spectra of the AlTiN (#1) and AlTiON samples (#4 and #5) and Figure 9 (a-c) the corresponding reflectance spectra, along with the fitted theoretical ones. For these samples one Lorentz and two Gauss oscillators were applied to fit the experimental data in the range from 211 nm – to 1688 nm and another 3 to 4 Lorentz oscillators for the extension into the IR range up to 25000 nm. This fitting procedure significantly improves the extrapolation performed by the simulation software and reported in the literature [57–59]. AlTiN (#1) was too absorptive to determine the thickness as there was no change in the model for thicknesses higher than 350 nm, meaning that light can only travel up to ~ 700 nm through this material without getting completely absorbed. Thicknesses / roughnesses of the other two samples were determined to be as follows: #4 ( $375 \pm 5$ ) nm / ( $6 \pm 2$ ) nm and #5 ( $380 \pm 5$ ) nm /

(12 ± 2) nm. The errors are estimated from gradually changing those parameters in the model fit and from the correlation with other fit parameters, although the highest correlation exists between thickness and roughness themselves.

Due to the need of a high-energy pole function it can be concluded that a major absorption is located outside the measured range on the high energy edge of the spectrum (> 5.8 eV), corresponding to  $\lambda < 213$  nm, which is most probably an interband transition of the AlTiO and AlTiN. This corresponds with the fact that AlN as well as Al<sub>2</sub>O<sub>3</sub> both have band gaps higher than this value [60–62].

The absorptions modelled by Gauss oscillators in the range of 3.0 – 6.0 eV (~ 200 to 400 nm) are assumed to be transitions related to defect states as their energies are high but their amplitudes are low compared to interband transitions. As defect states are distributed randomly regarding the energies of their transitions and the width of this distribution is orders of magnitude higher than the width of the transitions themselves, a statistical Gauss distribution of numerous harmonic oscillators is applicable. On the other hand, intraband transitions, with energies of 0.05 eV (24800 nm) – 1.87 eV (663 nm), are rather discrete so they were modelled by Lorentz oscillators. With regard to simplicity of the model, for these samples one homogeneous layer was assumed. In reality there is columnar growth (see Figure 3) which can explain small deviations of the optical model from the measured data as described in [63].

The SE and reflectance spectra of the AlTiO sample (#6) show totally different behaviour compared to the other samples (see Figure 8 ((d) and Figure 9 (d)). This material is considerably more transparent in the VIS range, resulting in a characteristic shape of the SE spectrum with more pronounced oscillations in psi and delta. Additionally, the IR reflectivity is not as high as in AlTiN and AlTiON. From the ERD spectrum (Figure 1 (f)) and the SEM cross section (Figure 3 (f)), of sample #6 it is evident that it is not one homogeneous layer but rather three layers with different ratios of Al, Ti and O. The top layer is characterized by a high O content of ~ 60 at.%, indicating presence of fully oxidized Al and Ti. The middle and bottom layers contain less oxygen (~ 50 at. % and 27 at. % respectively), indicating a certain amount of non-oxidized metals. Taking this into account a three layer effective medium approximation (EMA) model was developed containing different amounts of mostly Al<sub>2</sub>O<sub>3</sub>, but also TiO<sub>2</sub>, Al and Ti, related with the concentration obtained by the ERD analysis. Also, the depolarization factor of this Bruggeman-EMA [64] was determined to be ~ 0.33, pointing to spherical inclusions consistent with the SEM result (Figure 3 (f)). Thickness and roughness of this sample were determined to be (82 ± 3) nm / (4 ± 1) nm, respectively.

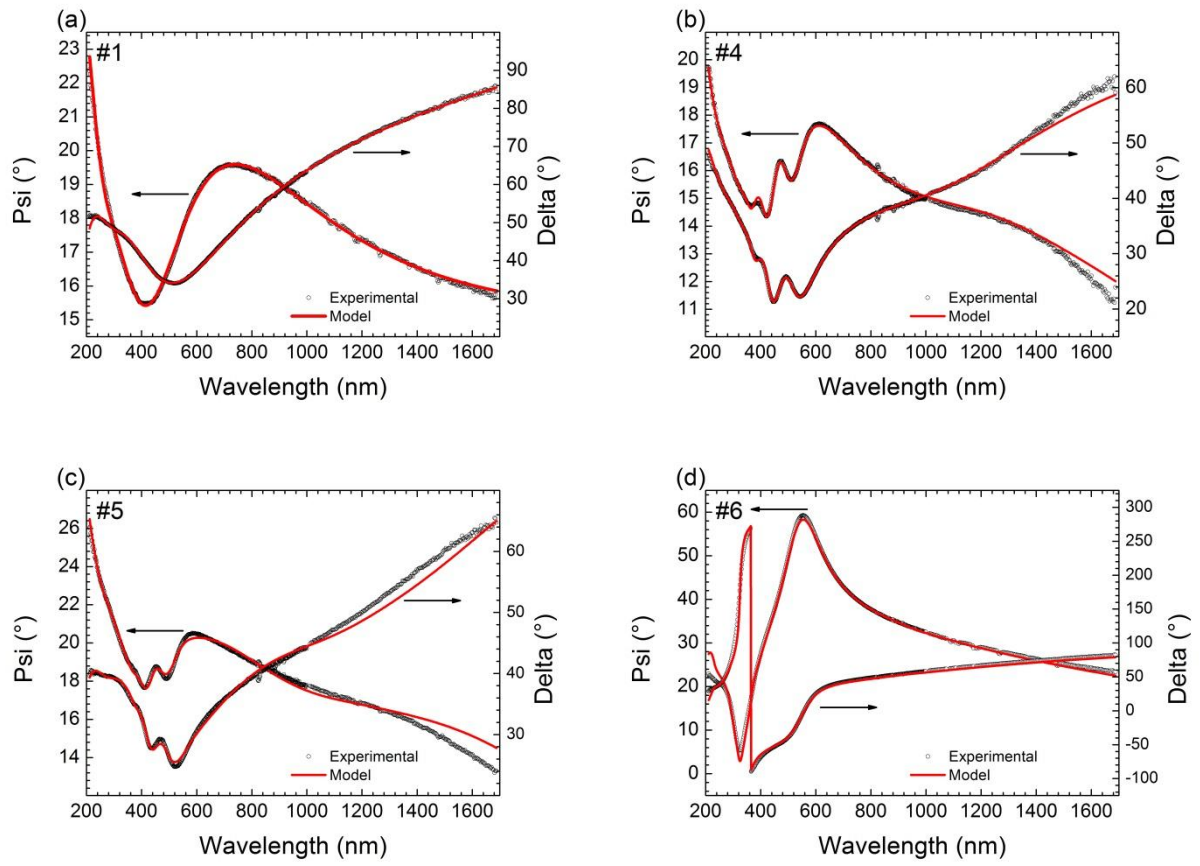
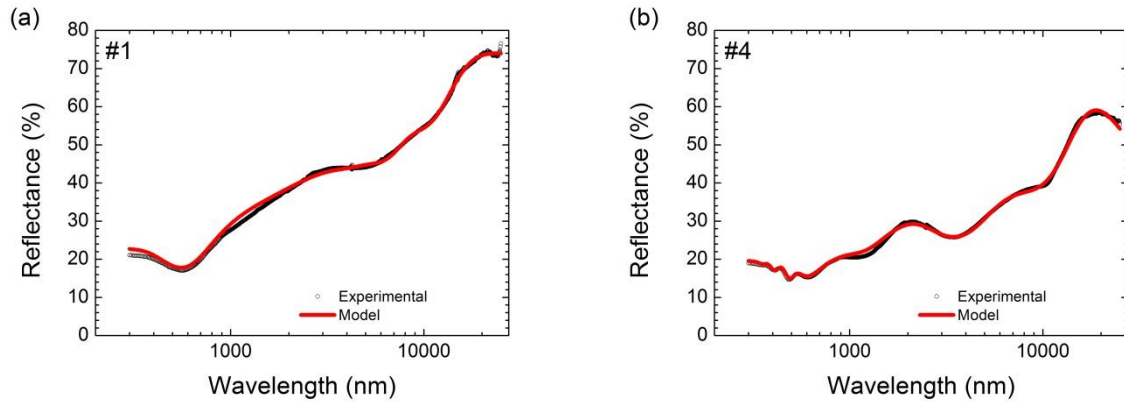


Figure 8: Experimental psi and delta along with fitted values for (a) AlTiN #1, (b) AlTiON #4, 14 at.% O (c) AlTiON #5, 20 at.% O and (d) AlTiO #6 samples deposited on silicon substrate.



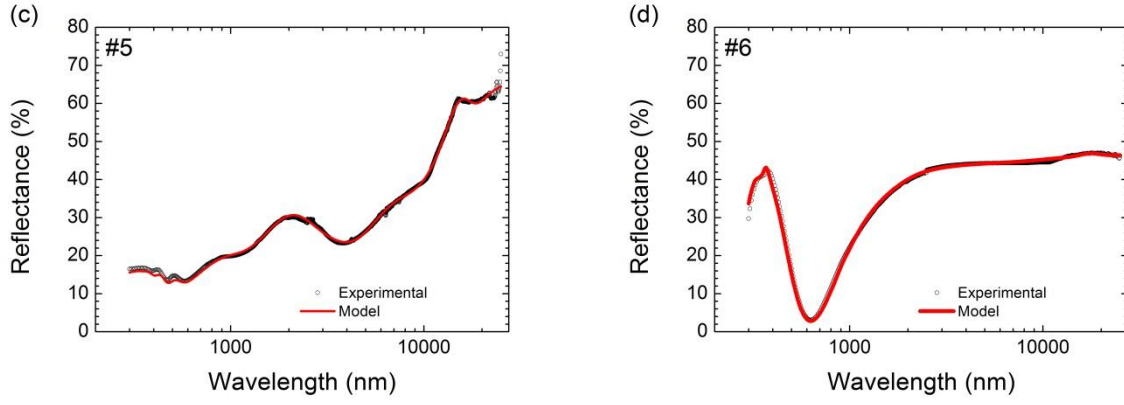


Figure 9: Experimental reflectance along with fitted values for (a) AlTiN #1, (b) AlTiON #4, 14 at.% O, (c) AlTiON #5, 20 at.% O and (d) AlTiO #6 samples deposited on silicon substrate.

The refractive index ( $n$ ) and extinction coefficient ( $k$ ) obtained from the above described optical models are shown in Figure 10. For the AlTiO sample (#6) there is no single layer but additionally a nucleation- and a surface oxide layer. The optical constants for each layer are different and not comparable to  $n$  and  $k$  of sample #1, #4 and #5. Therefore only those samples are compared in the following figure. Assuming the middle layer of sample #6 is crucial for this material, it can be said that its refractive index varying between  $1 < n < 2$  (for  $250 \text{ nm} < \lambda < 10000 \text{ nm}$ ) and  $2 < n < 2.25$  (for  $10000 \text{ nm} < \lambda < 25000 \text{ nm}$ ) as well as its extinction coefficient  $k < 0.35$  in the whole range, are smaller than for the other samples, which is desirable if the material should be used as anti-reflective coating.

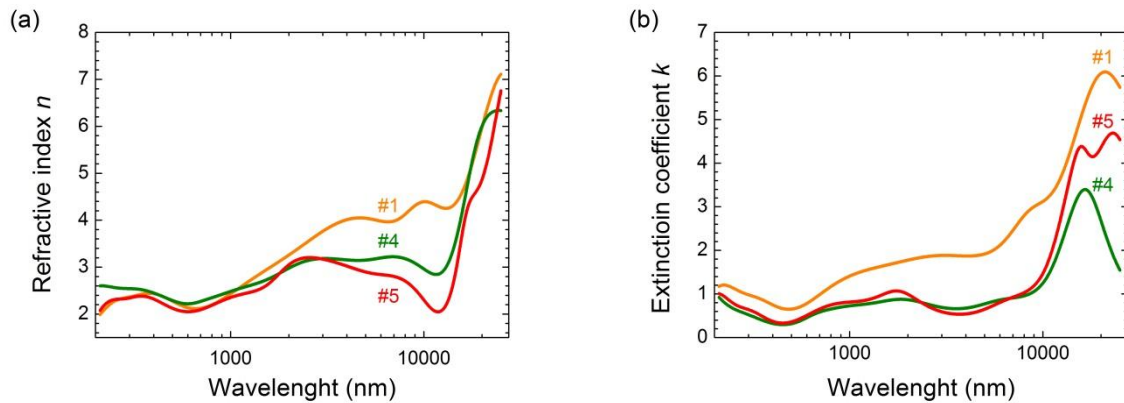


Figure 10: (a) Refractive index ( $n$ ) and (b) extinction coefficient ( $k$ ) after modelling the measured SE values of  $\text{Al}_y\text{Ti}_{1-y}(\text{O}_x\text{N}_{1-x})$  samples #1-#5 deposited on Si substrate.

The optical constants of all 3 samples are similar, especially in  $n$  where values range between 2 and 3 in the UV-Vis and NIR part of the spectrum are reasonable for mixtures of AlN ( $n \sim 2.3$  [65]),  $\text{Al}_2\text{O}_3$  ( $n \sim 1.65$  [66]), TiN ( $n \sim 2.5$  [67]) and  $\text{TiO}_2$  ( $n \sim 2.6$  [68]) and consistent with results obtained by Rebouta *et al.* [21] and Valkonen *et al.* [69] for AlTi(O)N and TiN respectively. Towards the infrared range the refractive indices increase considerably which is



a consequence of the increasing extinction due intraband transitions of the charge carriers, indicating metal-like behaviour in those materials. In the reflectance spectrum (Figure 9) this results in increasing reflectance above 10 $\mu$ m. The oxynitride samples (#4 and #5) exhibit an overall lower extinction coefficient compared to the pure nitride sample (#1), indicating a transition into dielectric behaviour which is consistent with the evolution of reflectance spectra from sample #1 - #6. The  $Al_yTi_{1-y}(O_xN_{1-x})$  layers present reasonably high extinction coefficients around 1 in the UV-Vis and NIR range.

This, concurrently with the above mentioned refractive indices, resulted in high absorption values of > 80 % (see Figure 9) already for single oxynitride layers of those materials. In particular, the combination of these layers with an anti-reflective coating confirms their suitability for sunlight absorption. The furthermore high IR reflectivity endorses solar-selective properties to such materials. Both, absorptivity and selectivity can be increased by multilayer structures consisting of those materials as shown in the next part.

### 3.5 Solar selective multilayers based on $Al_yTi_{1-y}(O_xN_{1-x})$ individual layers

Three different SSC (multilayer 1, 2 and 3), were designed using the optical constants of the single  $Al_yTi_{1-y}(O_xN_{1-x})$  layers modelled in section 3.4. The complete stacks were simulated to be deposited on 2 mm thick Inconel HAYNES ® 230 top-coated with a 400 nm TiN layer. The latter was used as infrared reflective layer whose  $n$  and  $k$  were experimentally measured in a previous work [34]. The number of  $Al_yTi_{1-y}(O_xN_{1-x})$  layers, the oxygen concentration and the layer thickness were optimized in order to maximize the solar absorptance and minimize the thermal emittance. The simulated reflectance spectra of the three configurations and the parameters employed for each one are schematized in Figure 11.

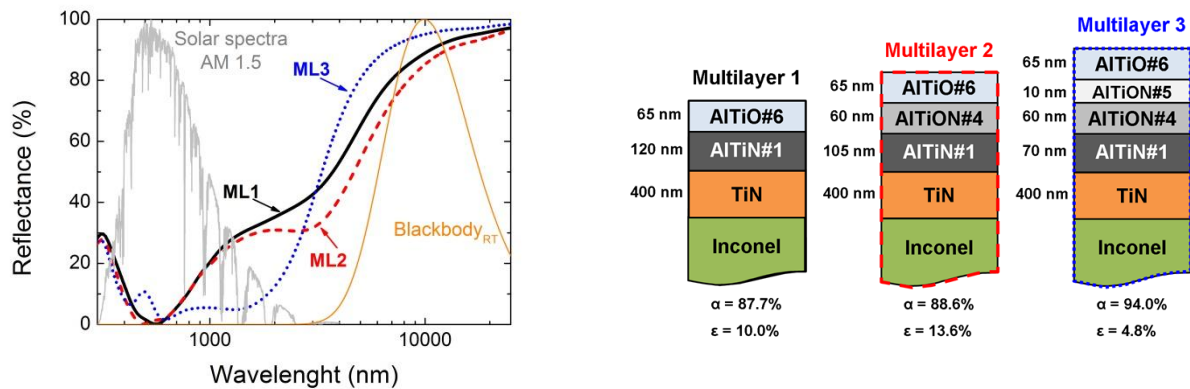


Figure 11: Specular reflectance obtained from CODE simulation of three different configurations: multilayer 1, 2 and 3. The description of the multilayer stacks and the simulated values obtained for the solar absorptance ( $\alpha$ ) and thermal emittance ( $\epsilon$ ) are included in the figure.

The simplest design of multilayer 1 comprises AlTiO #6/AlTiN #1/TiN layers. This design using only one absorbing AlTiN layer yielded  $\alpha = 87.7\%$  and  $\varepsilon_{RT} = 10.0\%$ . The addition of an intermediate oxynitride layer (sample #4) to the stack (multilayer 2) slightly increases  $\alpha = 88.6\%$  at the expense of the emittance ( $\varepsilon_{RT} = 13.6\%$ ). Finally, the best optical performance was achieved by employing a more complex design with 2 oxynitride layers with different oxygen content (samples #4 and #5) on top of the AlTiN. The selective performance achieved by this multilayer 3 ( $\alpha = 94.0\%$  and  $\varepsilon_{RT} = 4.8\%$ ) is among the best performing reported for simulated layer stacks using oxynitride films [18,35]. In a companion article [36] the experimental deposition and thermal stability of the designed multilayers will be demonstrated, pointing out these materials as real alternative beyond the state of the art in solar selective coating applications.

## 4 Conclusions

$\text{Al}_y\text{Ti}_{1-y}(\text{O}_x\text{N}_{1-x})$  single layers were comprehensively characterized with respect to their composition, morphology, phase and microstructure. Their optical properties were measured by three complementary methods. Optical models reproducing the experiments in the whole wavelength range from 190 nm to 25  $\mu\text{m}$  were used to design multilayer SSC stacks with excellent solar selectivity. These have great potential for high-temperature CSP central receiver plants.

The multilayer stacks can be deposited by a one-step CVA process by varying the gas composition in the chamber. Starting with an IR layer of TiN on Inconel, an  $\text{Al}_{0.67}\text{Ti}_{0.33}$  target can be sputtered with an increasing O/N ratio, thus increasing the oxygen content in the growing film. Within the composition range characterized by O/N ratios of  $\sim 0$  to 0.57 and the Al/Ti ratio of  $\sim 2$ , the same *fcc* phase structure as in the underlying TiN is formed. Simultaneously, the mean crystallite diameter decreases and the initially nanocrystalline columnar morphology changes stepwise into a mixture of nanocrystalline and amorphous fractions. These structural changes allow for quasi-epitaxial growth of the CSP absorber layer with good adhesion and a stable *fcc* structure, and moreover, improved oxidation resistance and optimized absorption. Finally, in the same process, an AR top layer with the nominal composition of  $\text{Al}_{0.75}\text{Ti}_{0.25}\text{O}_3$  and a  $\gamma\text{-Al}_2\text{O}_3$  phase structure can be deposited. This fully-oxidized and dense layer serves furthermore as oxidation protection for the SSC stack. Exhaustive simulation work of different  $\text{Al}_y\text{Ti}_{1-y}(\text{O}_x\text{N}_{1-x})$  SSC multilayers was performed in order to obtain trustful models for the reflectance based on optical constant measurements. In

this work, it is demonstrated that a solid understanding of the correlations between bonding type and composition is required in order to properly adjust the solar selective properties of high-temperature resistance oxynitride materials. A SSC composed of AlTiO / AlTiON (20at.%) / AlTiON (14at. %) / AlTiN / TiN exhibited an optimal  $\alpha = 94.0\%$  and  $\varepsilon_{RT} = 4.68\%$ .

## 5 Acknowledgments

This project was partially supported by H2020 RISE project “Framework of Innovation for Engineering of New Durable Solar Surfaces (FRIENDS<sup>2</sup>, GA-645725)”. Support by the Ion Beam Centre (IBC, Helmholtz-Zentrum Dresden-Rossendorf) is gratefully acknowledged. The authors would like to thank R. Heller (Helmholtz-Zentrum Dresden – Rossendorf) for assistance during the use of IBA at the IBC, A. Mayoral (Laboratorio de Microscopias Avanzadas from Instituto de Nanociencia de Aragón) for offering access to their instruments and expertise with TEM measurement, and M<sup>a</sup> C. Jiménez de Haro (Instituto Ciencia y Tecnología de Materiales de Sevilla) for the SEM service.

Any opinions, findings and conclusions or recommendations expressed in this material are those of the authors and do not necessarily reflect those of the host institutions or funders.

## 6 References

- [1] L.A. Weinstein, J. Loomis, B.B. Bhatia, D.M. Bierman, E.N. Wang, G.G. Chen, Concentrating Solar Power, *Chem. Rev.* 115 (2015) 12797.
- [2] Q.-C. Zhang, Recent progress in high-temperature solar selective coatings, *Sol. Energy Mater. Sol. Cells.* 62 (2000) 63–74.
- [3] N. Selvakumar, H.C. Barshilia, Review of physical vapor deposited (PVD) spectrally selective coatings for mid- and high-temperature solar thermal applications, *Sol. Energy Mater. Sol. Cells.* 98 (2012) 1–23.
- [4] S. Wijewardane, D.Y. Goswami, A review on surface control of thermal radiation by paints and coatings for new energy applications, *Renew. Sustain. Energy Rev.* 16 (2012) 1863–1873.
- [5] C.K. Ho, A.R. Mahoney, A. Ambrosini, M. Bencomo, A. Hall, T.N. Lambert, Characterization of Pyromark 2500 for High-Temperature Solar Receivers, in: *ASME 2012 6th Int. Conf. Energy Sustain. Parts A B*, ASME, 2012: p. 509.
- [6] H.L. Zhang, J. Baeyens, J. Degrève, G. Cacères, Concentrated solar power plants: Review and design methodology, *Renew. Sustain. Energy Rev.* 22 (2013) 466–481.
- [7] G.A. Niklasson, C.G. Granqvist, Review: Surfaces for selective absorption of solar energy: an annotated bibliography 1955-1981, *J. Mater. Sci.* 18 (1983) 3475–3534.
- [8] W.F. Bogaerts, C.M. Lampert, Materials for photothermal solar energy conversion, *J. Mater. Sci.* 18 (1983) 2847–2875.
- [9] P. Oelhafen, A. Schüler, Nanostructured materials for solar energy conversion, *Sol. Energy.* 79 (2005) 110–121.
- [10] F. Cao, K. McEnaney, G. Chen, Z. Ren, Review of Cermet-based Spectrally-Selective Solar Absorbers, *Energy Environ. Sci.* (2014).
- [11] J. Nohava, P. Dessarzin, P. Karvankova, M. Morstein, Characterization of tribological behaviour and wear mechanisms of novel oxynitride PVD coatings designed for applications at high temperatures, *Tribol. Int.* 81 (2015) 231–239.
- [12] H. Schellinger, M.P. Lazarov, H. Klank, R. Sizmann, Thermal and Chemical Metallic - Dielectric Transitions of TiN<sub>x</sub>O<sub>y</sub> Cu Absorber Tandems, in: C.M. Lampert (Ed.), *SPIE’s 1993 Int. Symp. Opt. Imaging, Instrum.*, International Society for Optics and Photonics, 1993: pp. 366–376.



- [13] H. Schellinger, M.P. Lazarov, W. Assmann, B. Bauer, C. Steinhausen, Improved selective properties of SiO<sub>2</sub>/TiNO/Al tandem absorbers effected by tempering, in: V. Wittwer, C.G. Granqvist, C.M. Lampert (Eds.), *Opt. Mater. Technol. Energy Effic. Sol. Energy Convers. XIII*, International Society for Optics and Photonics, 1994: pp. 172–181.
- [14] H.C. Barshilia, N. Selvakumar, K.S. Rajam, D.V. Sridhara Rao, K. Muraleedharan, Deposition and characterization of TiAlN/TiAlON/Si<sub>3</sub>N<sub>4</sub> tandem absorbers prepared using reactive direct current magnetron sputtering, *Thin Solid Films*. 516 (2008) 6071–6078.
- [15] H. Lei, D. Miao, L. XiaoPeng, W. ShuMao, J. LiJun, L. Fang, et al., Thermal stability of nitride solar selective absorbing coatings used in high temperature parabolic trough current, *Sci. China Technol. Sci.* 53 (2010) 1507–1512.
- [16] L. Rebouta, P. Capela, M. Andritschky, A. Matilainen, P. Santilli, K. Pischow, et al., Characterization of TiAlSiN/TiAlSiON/SiO<sub>2</sub> optical stack designed by modelling calculations for solar selective applications, *Sol. Energy Mater. Sol. Cells*. 105 (2012) 202–207.
- [17] K. Valleti, D. Murali Krishna, S.V. Joshi, Functional multi-layer nitride coatings for high temperature solar selective applications, *Sol. Energy Mater. Sol. Cells*. 121 (2014) 14–21.
- [18] Y. Wu, C. Wang, Y. Sun, Y. Xue, Y. Ning, W. Wang, et al., Optical simulation and experimental optimization of Al/NbMoN/NbMoON/SiO<sub>2</sub> solar selective absorbing coatings, *Sol. Energy Mater. Sol. Cells*. 134 (2015) 373–380.
- [19] J. Jyothi, H. Chaliyawala, G. Srinivas, H.S. Nagaraja, H.C. Barshilia, Design and fabrication of spectrally selective TiAlC/TiAlCN/TiAlSiCN/TiAlSiCO/TiAlSiO tandem absorber for high-temperature solar thermal power applications, *Sol. Energy Mater. Sol. Cells*. 140 (2015) 209–216.
- [20] H. Lei, W. ShuMao, J. LiJun, L. XiaoPeng, L. HuaLing, L. ZhiNian, Preparation and thermal stability on non-vacuum high temperature solar selective absorbing coatings, *Chinese Sci. Bull.* 54 (2009) 1451–1454.
- [21] L. Rebouta, A. Pitães, M. Andritschky, P. Capela, M.F. Cerqueira, A. Matilainen, et al., Optical characterization of TiAlN/TiAlON/SiO<sub>2</sub> absorber for solar selective applications, *Surf. Coatings Technol.* 211 (2012) 41–44.
- [22] H.C. Barshilia, N. Selvakumar, K.S. Rajam, Thermal stability of TiAlN/TiAlON/Si<sub>3</sub>N<sub>4</sub> tandem absorbers prepared by reactive direct current magnetron sputtering, *J. Vac. Sci. Technol. A Vacuum, Surfaces, Film*. 25 (2007) 383.
- [23] H.C. Barshilia, Growth, characterization and performance evaluation of Ti/AlTiAlTiNON/AlTiO high temperature spectrally selective coatings for solar thermal power applications, *Sol. Energy Mater. Sol. Cells*. 130 (2014) 322–330.
- [24] K.P. Sibin, S. John, H.C. Barshilia, Control of thermal emittance of stainless steel using sputtered tungsten thin films for solar thermal power applications, *Sol. Energy Mater. Sol. Cells*. 133 (2015) 1–7.
- [25] H.C. Barshilia, V.K.W. Grips, K.S. Rajam, Solar selective coating having higher thermal stability useful for harnessing solar energy and a process for the preparation thereof, US 7585568 B2, 2009.
- [26] H.C. Barshilia, R.C. Dhawan, An improved solar selective coating having high thermal stability and a process for the preparation thereof, WO2013088451A1, 2013.
- [27] H.C. Barshilia, J.B. Bharathibai, L.V. Ramachandrappa, A hybrid multilayer solar selective coating for high temperature solar thermal applications and a process for the preparation thereof, WO2014122667A1, 2014.
- [28] H. Najafi, A. Karimi, P. Dessarzin, M. Morstein, Correlation between anionic substitution and structural properties in AlCr(O<sub>x</sub>N<sub>1-x</sub>) coatings deposited by lateral rotating cathode arc PVD, *Thin Solid Films*. 520 (2011) 1597–1602.
- [29] S.G. Ebbinghaus, H.P. Abicht, R. Dronskowski, T. Müller, A. Reller, A. Weidenkaff, Perovskite-related oxynitrides - Recent developments in synthesis, characterisation and investigations of physical properties, *Prog. Solid State Chem.* 37 (2009) 173–205. doi:10.1016/j.progsolidstchem.2009.11.003.
- [30] J. Sjöln, L. Karlsson, S. Braun, R. Murdey, A. Hörling, L. Hultman, Structure and mechanical properties of arc evaporated Ti–Al–O–N thin films, *Surf. Coatings Technol.* 201 (2007) 6392–6403. doi:10.1016/j.surfcoat.2006.12.
- [31] C. Nunes, V. Teixeira, M.L. Prates, N.P. Barradas, A.D. Sequeira, Graded selective coatings based on chromium and titanium oxynitride, *Thin Solid Films*. 442 (2003) 173–178.
- [32] J. Borges, F. Macedo, F.M. Couto, M.S. Rodrigues, C. Lopes, P. Pedrosa, et al., The influence of nitrogen and oxygen additions on the thermal characteristics of aluminium-based thin films, *Mater. Chem. Phys.* 163 (2015) 569–580.
- [33] R. Luthier, F. Levy, Magnetron sputtered TiAlON composite thin films. II. Optical and electrical properties, *J. Vac. Sci. Technol. A Vacuum, Surfaces, Film*. 9 (1991) 110.
- [34] I. Heras, M. Krause, G. Abrasonis, A. Pardo, J.L. Endrino, E. Guillén, et al., Advanced characterization and optical simulation for the design of solar selective coatings based on carbon: transition metal carbide nanocomposites, *Sol. Energy Mater. Sol. Cells*. 157 (2016) 580–590.
- [35] N. Selvakumar, K. Prajith, A. Biswas, H.C. Barshilia, Optical simulation and fabrication of HfMoN/HfON/Al<sub>2</sub>O<sub>3</sub> spectrally selective coating, *Sol. Energy Mater. Sol. Cells*. 140 (2015) 328–334.
- [36] I. Heras, E. Guillén, F. Lungwitz, G. Rincón-Llorente, I. Azkona, M. Krause, et al., Design of high temperature solar-selective coatings based on aluminium titanium AlTi(O<sub>x</sub>N<sub>1-x</sub>) oxynitrides. Part 2: Durability tests at high temperature. (to be submitted)
- [37] J.M. Andersson, J. Vetter, J. Müller, J. Sjöln, Structural effects of energy input during growth of Ti<sub>1-x</sub>Al<sub>x</sub>N (0.55≤x≤0.66) coatings by cathodic arc evaporation, *Surf. Coatings Technol.* 240 (2014) 211–220.
- [38] H. Najafi, A. Karimi, P. Dessarzin, M. Morstein, Formation of cubic structured (Al<sub>1-x</sub>Cr<sub>x</sub>)<sub>2</sub>O<sub>3</sub> and its dynamic transition to corundum phase during cathodic arc evaporation, *Surf. Coatings Technol.* 214 (2013) 46–52.
- [39] N.P. Barradas, C. Jeynes, R.P. Webb, Simulated annealing analysis of Rutherford backscattering data, *Appl. Phys. Lett.* 71 (1997) 291.
- [40] B.D. Cullity, S.R. Stock, *Elements of X-ray diffraction*, Prentice-Hall, 2001.
- [41] J.A. Woollam, *Guide to using WVASE32*, Lincoln NE, New York, USA, 2010.
- [42] W. Theiss, *CODE Manual. Optical Spectrum Simulation*, (2007). <http://www.wtheiss.com/>.

- [43] ASTM, ASTM G173: Standard Tables for Reference Solar Spectral Irradiance at Air Mass 1.5: Direct Normal and Hemispherical for a 37 Degree Tilted Surface, US, 2008.
- [44] J.A. Duffie, W.A. Beckman, Solar engineering of thermal processes., 3rd ed., John Wiley & Sons, New York, 2005.
- [45] E. Standard, N. Europeenne, UNE-EN 673 Determinación del coeficiente de transmisión térmica, Europe, 2011.
- [46] R. Behrisch, S. Grigull, U. Kreissig, R. Grötzschel, Influence of surface roughness on measuring depth profiles and the total amount of implanted ions by RBS and ERDA, Nucl. Instruments Methods Phys. Res. Sect. B Beam Interact. with Mater. Atoms. 136-138 (1998) 628–632.
- [47] A.L. Patterson, The Scherrer Formula for X-Ray Particle Size Determination, Phys. Rev. 56 (1939) 978.
- [48] S. Kassavetis, G. Abadias, G. Vourlias, G. Bantsis, S. Logothetidis, P. Patsalas, Optical properties of  $Ti_xAl_{1-x}N$  thin films in the whole compositional range, Surf. Coatings Technol. (2015).
- [49] A. Hörling, L. Hultman, M. Odén, J. Sjöln, L. Karlsson, Thermal stability of arc evaporated high aluminium-content  $Ti_{1-x}Al_xN$  thin films, J. Vac. Sci. Technol. A Vacuum, Surfaces, Film. 20 (2002) 1815.
- [50] J.C. Schuster, J. Bauer, The ternary system titanium-aluminium-nitrogen, J. Solid State Chem. 53 (1984) 260–265.
- [51] C. Ducros, C. Cayron, F. Sanchette, Multilayered and nanolayered hard nitride thin films deposited by cathodic arc evaporation. Part 1: Deposition, morphology and microstructure, Surf. Coatings Technol. 201 (2006) 136–142.
- [52] K. Tönshoff, B. Karpuschewski, A. Mohlfeld, T. Leyendecker, G. Erkens, H. Fuß, et al., Performance of oxygen-rich TiAlON coatings in dry cutting applications, Surf. Coatings Technol. 108-109 (1998) 535–542.
- [53] A. Pélisson-Schecker, H.J. Hug, J. Patscheider, Morphology, microstructure evolution and optical properties of Al-Si-N nanocomposite coatings, Surf. Coatings Technol. 257 (2014) 114–120.
- [54] M. Fox, Optical Properties of Solids, Oxford Mas, Oxford University Press, Oxford, 2001.
- [55] R. Perrem, F. Henry, G. Peraudeau, B. Armas, R. Berjoan, E. Beche, An XPS and thermogravimetric study of oxidized AlN and AlN-Si<sub>3</sub>N<sub>4</sub> layers deposited by liquid-phase chemical vapour deposition, J. Mater. Sci. 32 (1997) 1305–1312.
- [56] L. Rebouta, A. Sousa, P. Capela, M. Andritschky, P. Santilli, A. Matilainen, et al., Solar selective absorbers based on Al<sub>2</sub>O<sub>3</sub>:W cermet and AlSiN/AlSiON layers, Sol. Energy Mater. Sol. Cells. 137 (2015) 93–100.
- [57] Q.-C. Zhang, Optimizing analysis of W-AlN cermet solar absorbing coatings, J. Phys. D. Appl. Phys. 34 (2001) 3113–3120.
- [58] J.H. Schön, E. Bucher, Computer modeling of the performance of some metal/dielectric multilayers for high-temperature solar selective absorbers, Sol. Energy Mater. Sol. Cells. 43 (1996) 59–65.
- [59] M. Farooq, Z.H. Lee, Computations of the optical properties of metal/insulator-composites for solar selective absorbers, Renew. Energy. 28 (2002) 1421–1431.
- [60] W.L. OBrien, J. Jia, Q.Y. Dong, T.A. Callcott, J.E. Rubensson, D.L. Mueller, et al., Intermediate coupling in L2-L3 core excitons of MgO, Al<sub>2</sub>O<sub>3</sub>, and SiO<sub>2</sub>, Phys. Rev. B. 44 (1991) 1013–1018.
- [61] M. Feneberg, R.A.R. Leute, B. Neuschl, K. Thonke, M. Bickermann, High-excitation and high-resolution photoluminescence spectra of bulk AlN, Phys. Rev. B - Condens. Matter Mater. Phys. 82 (2010) 1–8.
- [62] C.H. Chen, J. Silcox, Surface guided modes in an aluminium oxide thin film, Solid State Commun. 17 (1975) 273–275.
- [63] A. Schüller, P. Reimann, P. Oelhafen, G. Francz, T. Zehnder, M. Duggelin, et al., Structural and optical properties of titanium aluminum nitride films ( $Ti_{1-x}Al_xN$ ), J. Vac. Sci. Technol. A. 19 (2001) 922.
- [64] D. Bruggeman, Calculation of various physics constants in heterogeneous substances I Dielectricity constants and conductivity of mixed bodies from isotropic substances, Ann. Phys. 24 (1935) 636–664.
- [65] J. Pastrnak, L. Roskovcova, Refraction Index Measurements on AlN Single Crystals, Phys. Status Solidi. 14 (1966) K5–K8.
- [66] P. Kumar, M.K. Wiedmann, C.H. Winter, I. Avrutsky, Optical properties of Al<sub>2</sub>O<sub>3</sub> thin films grown by atomic layer deposition, Appl. Opt. 48 (2009) 5407.
- [67] J. Pflüger, J. Fink, W. Weber, K. Bohnen, G. Crecelius, Dielectric properties of TiC<sub>x</sub>, TiN<sub>x</sub>, VC<sub>x</sub>, and VN<sub>x</sub> from 1.5 to 40 eV determined by electron-energy-loss spectroscopy, Phys. Rev. B. 30 (1984) 1155–1163.
- [68] T.E. Tiwald, M. Schubertb, Measurement of rutile TiO<sub>2</sub> dielectric tensor from 0.148 to 33 um using generalized ellipsometry, in: SPIE Proc. Opt. Diagnostic Methods Inorg. Mater. II, 2000: pp. 19–29.
- [69] E. Valkonen, C.-G. Ribbing, J.-E. Sundgren, Optical constants of thin TiN films: thickness and preparation effect, Appl. Opt. 25 (1986) 3624.